

Lightweight integration of 3D features to improve 2D image segmentation

Olivier PRADELLE^{c,**}, Raphaëlle CHAINE^c, David WENDLAND^d, Julie DIGNE^c

^aLIRIS, CNRS, Université Lyon 1

^bTechmodigit, 14 Porte du Grand Lyon, Neyron 01700, France

ABSTRACT

Scene understanding is a major challenge of today’s computer vision. Center to this task is image segmentation, since scenes are often provided as a set of pictures. Nowadays, many such datasets also provide 3D geometry information given as a 3D point cloud acquired by a laser scanner or a depth camera. To exploit this geometric information, many current approaches rely on both a 2D loss and 3D loss, requiring not only 2D per pixel labels but also 3D per point labels. However obtaining a 3D groundtruth is challenging, time-consuming and error-prone. In this paper, we show that image segmentation can benefit from 3D geometric information without requiring any 3D groundtruth, by training the geometric feature extraction with a 2D segmentation loss in an end-to-end fashion. Our method starts by extracting a map of 3D features directly from the point cloud by using a lightweight and simple 3D encoder neural network. The 3D feature map is then used as an additional input to a classical image segmentation network. During training, the 3D features extraction is optimized for the segmentation task by back-propagation through the entire pipeline. Our method exhibits state-of-the-art performance with much lighter input dataset requirements, since no 3D groundtruth is required.

This paper is under consideration at Computer Vision and Image Understanding.

1. Introduction

Today’s 3D scanners are often equipped with cameras acquiring RGB pictures alongside the 3D data: 2D images provide colors and texture of the objects, while 3D data provides geometric relationships between objects in the scene, beyond their differences in color and texture. In real-world scans, geometric information is sparse and often does not account for parts of the scene, due to object occlusions. These missing parts, however, might still be visible in one of the images. On the other hand, 2D images are affected by light variations and shadows but also by the settings of the camera (blur, etc). Hence, adequately combining both types of data can leverage their respective advantages and help overcome their limitations (Dai and Nießner, 2018; Hu et al., 2021).

Many datasets containing images and 3D information (ScanNet (Dai et al., 2017a), 2D-3D-S (Armeni et al., 2017)) provide both 2D and 3D groundtruth labels, these datasets being usually prepared and labelled manually. For the ScanNet dataset, the 3D instance segmentation was crowd-sourced to more than 500 coworkers (Dai et al., 2017a), using a specifically designed labelling interface, with CAD model alignments. This shows that the 3D groundtruth labelling task is highly non trivial to set up and work-intensive. On the contrary labelling 2D images is much simpler, as it can rely on traditional image segmentation techniques with a user possibly merging or correcting the

segmented parts and naming them.

In this context, we introduce a segmentation method exploiting both 2D and 3D information, able to remove all dependency on a 3D groundtruth, only relying on 2D labels. A lightweight encoder extracts features from a 3D point set which are used to improve 2D segmentation results, using a single view.

2. Related Work

2D image segmentation. 2D semantic segmentation has known several improvements over the last decade. (Long et al., 2014) replaced the last layers of a convolutional classification network (Krizhevsky et al., 2012) with fully connected layers to produce per pixel segmentation. (Ronneberger et al., 2015) alternatively proposed U-Net, an architecture that shares information between coarsest and finest representation layers, making it more robust to missing groundtruth data. Some approaches exploited even deeper networks (Szegedy et al., 2014) while others worked on the receptive fields of the convolution operation in order to achieve better context understanding. In particular, (Yu and Koltun, 2015) and (Chen et al., 2017) used dilated convolution (or atrous convolution) to gain contextual information. (Dai et al., 2017b) introduced a deformable convolution to allow the network to be more accurate in the area of interest.

Deep Learning for 3D point cloud segmentation. The main challenge of such sparse and unstructured data lies in the definition of a convolution operator working on points’ neighborhoods, robust to point permutation, sampling changes and

**Corresponding author:

e-mail: olivier.pradelle@liris.cnrs.fr (Olivier PRADELLE)

geometric transformations. To overcome the lack of structure and define a convolution operation in 3D, some methods discretize the point cloud on a voxel grid and use 3D convolutional neural networks (CNNs) (Choy et al., 2019; Liu et al., 2019) on such grids, while others rely on a nearest neighbor graph (Wang et al., 2018) or use ball neighborhood queries (Thomas et al., 2019).

To alleviate the need for a well-defined neighborhood, PointNet (Qi et al., 2016) relies on per point convolutions with shared weights and symmetric aggregation operators to work on the raw point cloud directly. The network is then robust to sampling changes and point permutation, but at the cost of losing the locality of the computations. PointNet++ (Qi et al., 2017) re-introduced some locality to the network, by using a multiscale computation. Other specific convolutions include defining the convolution weights as a continuous function on the local coordinates of 3D points (Wu et al., 2018), or centering a convolution kernel around each point and defining the kernel features by summing the point features lying in the kernel’s domain (Hua et al., 2017). Another way of handling 3D data is by projecting it to several 2D grids in a multi-view setting. (Boulch et al., 2017) and (Kundu et al., 2020) use a reconstructed mesh and render it from a free viewpoint. The rendered image is fed to a 2D semantic segmentation network, the predicted labels are projected back to the 3D points and merged across views. However, the mesh reconstruction process can be a costly step for large scenes.

Merging 2D and 3D data for scene segmentation. Combining 2D and 3D data can improve scene segmentation results by overcoming the limitation of each type of data. (Gupta et al., 2014) encode depth with RGB images and feed it to a segmentation network. But depth maps depend on the point of view, and cannot account for the whole geometry of the scene, because of occlusions. Another way to add 3D information to the 2D segmentation network is to weight the convolution operator by local depth adequately (Wang and Neumann, 2018). Similarly, (Cao et al., 2021) redefine a convolution operator for RGBD images to embed the shape variation in the image. CMX (Liu et al., 2022) uses a transformer network for RGB and depth images, merging both modalities between each encoder layer and using it during the decoding step as residual information. (Liu et al., 2021) use features extracted from point clouds by a 3D network as cues and train the 2D network to emulate those 3D features. This allows the 2D network to produce more informative features for the 2D segmentation. A crucial question when merging 2D and 3D features lies in where this merging should take place. One can either feed a combination of 2D and 3D information to a network (*early merge*), or combine features in deeper layers, such as the bottleneck (*late merge*). For 3D point cloud segmentation, (Jaritz et al., 2019; Dai and Nießner, 2018) use 2D features extracted by a 2D network working on multiple views as additional features to enhance a point set before feeding it to a segmentation network. They showed that this early merge gives better result than a late merging strategy, as it improves the propagation of the information from the images to the 3D data.

Merging information at several depths of CNNs has also been

explored. (Su et al., 2018) reconstruct a point set by multiview stereo, encode it in a voxel grid through a 3D CNN and project the encoded point set on a 2D grid. Because of the multiview reconstruction, each 3D point projects on a pixel and a standard 2D convolution can then be applied to the merged features at several depth in the 2D segmentation network. This method produces good results for object part segmentation, but does not scale well to large scenes. For more generic input point sets, BP-Net (Hu et al., 2021) similarly encode 2D pixel and 3D voxels data independently, then merge the representations at several layer depths during the decoding process. However, in that case, interleaving voxel with pixel representations is not so straightforward. Indeed, the area of a voxel projected in an image depends on its distance to the image, hence no exact correspondence can be found.

All these methods 2D-3D combined approaches require a large amount of memory during training, and many require a 3D groundtruth.

3. Overview

Given a dataset containing a 3D point cloud and registered 2D images, we propose a network architecture to segment 2D images into semantic classes. The process is single view: each image is segmented independently of the others by using a lightweight image segmentation network whose 2D input is enhanced by the output of a 3D point set encoder. During training, our network is only supervised by 2D images segmentation groundtruth.

To summarize, our main contributions are:

- A simple framework that takes a 3D point cloud and a single image and produces the image semantic segmentation in an end-to-end manner, improving the segmentation performance of several state-of-the-art image classifiers.
- A way to extract per view geometric information as a 2D map, much more informative than depthmaps.
- A way to exploit 3D information without requiring any 3D groundtruth.

4. Approach

The goal of our method is to predict a semantic segmentation of a real-world RGB image by exploiting both RGB and 3D geometric information provided by an additional point cloud registered with the image. The architecture of our network can be seen in Figure 1. It outputs a label for every input pixel.

First, a 3D encoder network processes the point set, and extracts 3D features per point. Since the camera pose is known, the 3D encoder can focus on the points located in the camera field of view, whether they are occluded or not. The advantage of having a point cloud of the scene, rather than a depth image, is that the geometric information is not only computed from the visible points, but also from the points occluded in the view, as they give valuable context information (see ablation study in the supplementary). We then project the 3D features onto

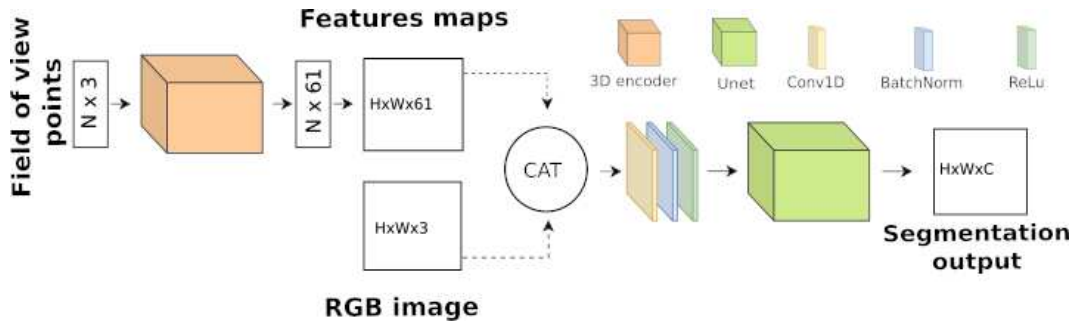


Fig. 1. The network takes as input a point cloud, an image and the corresponding projection matrix. The point cloud is processed using a 3D encoder architecture to extract per point features that are projected on a 2D geometric feature map in the view. The RGB image and the geometric feature map are merged using a single layer MLP before feeding it to a 2D convolutional architecture.

the image plane using the camera parameters, creating a 61-channel feature map. This feature map is view-dependent and can be thought of as an alternative to a depth map, encoding much richer geometric information. We proceed to merge this feature map with the RGB images. The final step is to feed the combined image to a standard 2D image segmentation network to predict per pixel segmentation.

To train our network we use a cross entropy loss between the predicted labels and the ground truth image pixel labels. During training, we optimize not only the weights of the 2D segmentation network but also the weights of the 3D encoder network and the weights of the merging operation, guided solely by the 2D ground truth segmentation. This allows the 3D network to optimize the features for the 2D segmentation task.

4.1. Per view 3D feature map

We chose to work directly on the raw point cloud to avoid any early discretization, as induced for example by a voxel grid, and to avoid costly preprocessing steps, such as mesh reconstruction.

Two widely used approaches that operate directly on raw point clouds are PointNet (Qi et al., 2016, 2017) and KPConv-CNN (Thomas et al., 2019). Our method can work with both these networks. However our experiments (section 6) show that KPConv CNN is too memory-demanding due to the sheer number of points in the field of view of an image, requiring to down-sample the point cloud. On the contrary, PointNet is a very light network, which turned out to produce better features. Hence we use PointNet by default.

We made a substantial change to the PointNet architecture: we removed the spatial transformers both in the 3D space and in the feature space. Since we express the points coordinates with respect to the camera coordinate system, which is relevant in our case, we do not need to find an optimal global coordinate system. The relevance of this modification is demonstrated in our ablation study (Section 6.4). This lighter PointNet can be seen in the Figure 2 and we refer to it as LPointNet (for light PointNet) in the remainder of the paper.

The output of our view specific 3D encoder is a 61-channel feature vector per point. We use it to create a 61-channel feature map by projecting the features of the visible points onto the image plane, using the camera parameters. The visibility of a point is obtained using a classical occlusion test for point

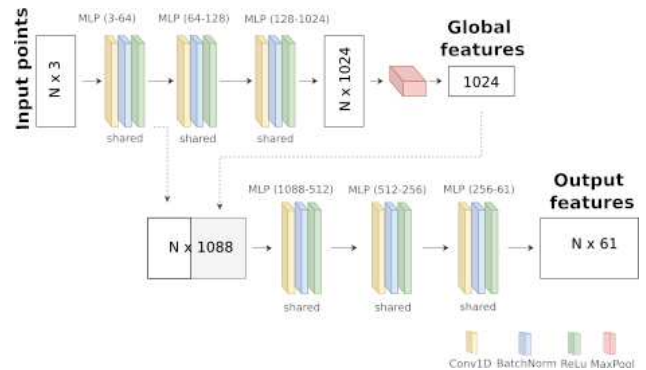


Fig. 2. Modified PointNet encoder. The spatial transformers are removed from the original architecture, as the frustum point cloud is expressed in the coordinate system of the camera.

sets (Pintus et al., 2011). Although only the features of visible points are kept, they also account for the geometry of relevant occluded points.

In practice, we do not rely on any pretrained weights for the 3D backbone (LPointNet or KPConv) and train it from scratch in an end-to-end manner. The ablation study also assesses the impact of this choice.

4.2. Combining the 3D features and RGB values

We locally merge the feature map with the color values pixelwise by concatenating the channels from the features map and the RGB image. The resulting 64 channels is then fed to a 1D convolution layer, with batchnorm and ReLU. In case no point projects on a pixel, we directly use a 1x1 convolution to map the 3-channel color information to 64 channels. This yields a combined 64-channel image which is processed by a standard 2D image segmentation network to predict per pixel segmentation. This merging step is shown as the layer between the 3D encoder and U-Net in Figure 1.

4.3. 2D backbone

We use standard networks for the 2D segmentation neural network: U-Net (Ronneberger et al., 2015) (with ResNet-34 (He et al., 2015) or ResNet-50 (He et al., 2015) encoders) or a DeeplabV3 (Chen et al., 2017), the U-net Resnet34 being by far the lighter architecture that we favor. The only difference with

the *vanilla* versions of these networks is that they are adapted to take 64-channel images instead of classical RGB images as input. In practice, the 2D encoders were pretrained on the ImageNet dataset (Russakovsky et al., 2015), with the exception of the first convolution layer, since it takes a 64-channel input instead of a 3-channel input. These first layer weights are initialized randomly.

5. Training

We applied our segmentation method to 4 standard datasets providing 2D images and a geometric information either as a point cloud (ScanNet (Dai et al., 2017a), 2D-3D-S (Armeni et al., 2017)), Kitty-360 (Liao et al., 2021) or as separate depth information for all views (NYU-V2 (Nathan Silberman and Fergus, 2012)). More details on the preprocessing steps of these datasets can be found in the supplementary material. All these datasets provide 2D images of groundtruth per pixel labels.

The network was trained with a Stochastic Gradient Descent (SGD) optimizer for 40 epochs. To stabilize the learning, we divide the learning rate by 2 every 5 epochs, which we have found to give satisfactory results. We use an initial learning rate of 0.01 with a weight decay of 0.0001 and a momentum of 0.9.

6. Experiments

All our experiments were run on a computer with an Nvidia RTX quadro 6000 gpu.

6.1. ScanNet validation dataset

We tested our method on the validation set of the ScanNet dataset (Dai et al., 2017a) and compare our results with state of the art methods (Table 1). The scores for SSMA, 3D-to-2D, RF-Net and VirtualMV were taken from the papers, while CMX was retrained, since the scores on the validation dataset were not provided. We also retrained BP-Net approach. We report in this table the number of parameters of each method, taken from the official github repositories when they are available.

Our method gives better results than single view RGBD based methods (Deng et al., 2019; Valada et al., 2019), even with a lighter 2D encoder (ResNet34 in our case compared to ResNet50). This indicates that combining 3D and 2D features is more powerful than 2.5D features, even without explicit 3D supervision.

Virtual MV fusion (Kundu et al., 2020) exhibits the best performance. However, the key factor for these high scores lies in the heavy data augmentation technique used at training. Synthetic images from a reconstructed scene mesh are generated, in a free-viewpoint manner and with a larger field of view.

In the case of BP-Net (Hu et al., 2021), the final prediction is obtained by aggregating multiple predictions for an image. We trained the network provided by the official github repository on 2 GPU for the comparison to be meaningful. Compared to BP-Net, our method does not require 3D groundtruth. It also

avoids any discretization step, since we process the point cloud directly instead of a set of voxels.

Adding either 3D backbones (LPointNet or KP-Conv) to a standard 2D backbone still keeps the number of parameters below other state of the art methods. As a result, our approach requires less memory, both during training and at inference time. The proposed method can thus run on a single low-end GPU. Table 2 presents the number of parameters and the training times of some of the most efficient methods, with available codes, on the ScanNet dataset. The number of parameters was obtained using the official repositories on github.

Figure 7 illustrates the improvement of the segmentation results compared to the 2D baseline. As it can be seen on the image, the 3D features extracted from the point clouds allow the network to add consistency between the predicted pixel class and the object on the image. It also tends to better preserve the object’s boundaries, as the 3D data allows to capture the object shape.

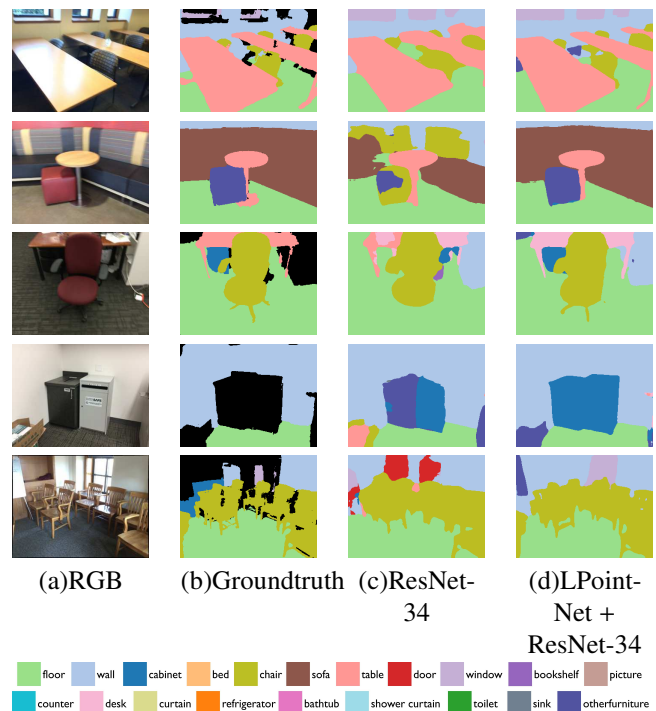


Fig. 3. Segmentation result on the ScanNet validation dataset. Merging the images with 3D information allows the network to predict more accurate object boundaries compared to the 2D baseline (U-Net34.)

3D features contribution. To assess the contribution of our optimized 3D features, we compare our results with a same network working on RGB, RGBD and RGBXYZ data. Results are reported in Table 3 and show that adding 3D features significantly improves the segmentation (+10% mIoU). The fact that using our feature map instead of an RGBD image improves the segmentation by a large margin is particularly informative since depth images are denser than our feature maps. Despite our sparser geometric information, the final segmentation is quantitatively improved, illustrating that our 3D feature extraction does more than simply computing a spatial information. Fi-

Table 1. Comparison on the ScanNet validation set, with state-of-the-art single view methods including RGBD methods (marked with a *) and 2D-3D based approaches using a 3D groundtruth (marked with **). Some methods do not provide their implementation and do not report the total number of parameters.

| Methods | InputType | GT | NbParam | 2D backbone | mIoU |
|-----------------------------------|-----------------------------|-------|-------------|--------------|-------------|
| SSMA* (Valada et al., 2019) | RGB + Depth (HHA) | 2D | 30.2 M | Resnet50 | 52.9 |
| 3D-to-2D distil Liu et al. (2021) | RGB + Point cloud | 2D | 66M | Resnet50 | 58.2 |
| CMX (Liu et al., 2022) | RGB + Depth (HHA) | 2D | 66 M | SegFormer-B2 | 61.0 |
| RFBNet* (Deng et al., 2019) | RGB + Depth (HHA) | 2D | No info | Resnet50 | 62.6 |
| Ours (KPCConv + U-Net34) | RGB + Point cloud | 2D | 49 M | Resnet34 | 63.8 |
| BPNet** (Hu et al., 2021) | RGB + Point cloud | 2D/3D | 96 M | Resnet34 | 64.4 |
| Ours (LPointNet + U-Net34) | RGB + Point cloud | 2D | 26 M | Resnet34 | 66.1 |
| VirtualMV** (Kundu et al., 2020) | RGB + Normals + Coordinates | 3D | No info | xception65 | 67.0 |

Table 2. Memory consumption of the training step on the ScanNet dataset. We could not report the information for Virtual MV fusion since there is no official code available.

| Methods | NbParam | GPU Memory | Training time |
|---------|---------|----------------------|---------------|
| CMX | 66M | 2080Ti (4x11Gb) | 3 days |
| BPNet | 96M | RTX6000 (4x48Gb) | 2 days |
| Ours | 26M | RTXQuadro6000 (24Gb) | 1,5 days |

nally, we experiment a different way of merging 2D and 3D information, by processing RGB and depth independently, using two dedicated U-Nets and merging the information at the bottleneck only. Even compared to this configuration, our approach achieves significant improvement in terms of mIoU scores, with a very reasonable memory impact. The LPointNet + U-Net approach only adds 1M parameters to the architecture (26M parameters), while the dedicated U-Net almost doubles the total number of parameters (46M parameters). In all these experiments, we used a ResNet-34 encoder for U-Net.

Table 3. 2D mIoU on the validation set of the ScanNet dataset, for 2D U-Net segmentation networks based either on RGB images, RGBD images or for our method (* denote the addition of data augmentation).

| Methods | mIoU | mIoU gain |
|------------------------------------|-------------|--------------|
| U-Net34 (RGB) | 55.5 | |
| U-Net34 (RGBD) | 59.3 | +3.8 |
| U-Net34 (RGB) + U-Net34 (D) | 61.2 | +5.7 |
| U-Net34 (RGB) + U-Net34 (xyz img) | 62.3 | +6.8 |
| KPCConv + U-Net34 (Ours) | 63.8 | +8.3 |
| LPointNet + U-Net34 (Ours) | 65.4 | +9.9 |
| LPointNet + U-Net34 (Ours)* | 66.1 | +10.6 |

6.2. 2D-3D-S dataset

Following the procedure recommended in Armeni et al. (2017), we used the images from Area_5 as validation data, while the other areas were used to train the network. The data was preprocessed following the approach described in the supplementary. As the 3D pointset covers the whole floor and does

not restrict to a single room, we use the provided depth map to filter out points belonging to other rooms, to reduce memory usage, as they are not relevant to the RGB image. We used the same set of hyperparameters as for the ScanNet dataset during training. We compare our 2D segmentation result with other methods on Table 4.

Compared to the 2D baseline (U-Net34), our approach improves the mIoU scores by more than 10%. This shows that using 3D data significantly helps the network to produce better segmentation result. Among the methods which processes point clouds with RGB images, our approach outperforms Liu et al. (2021) which uses the same 2D backbone as ours. Our improvement can be explained by the fact that we use real 3D data, while Liu et al. (2021) only mimic 3D features. CMX (Liu et al., 2022) yields a better score than ours, but at the price of a much heavier 2D backbone (SegFormer-B4 (Xie et al., 2021)), with six times more parameters. The performance gain with respect to the increase in memory consumption is still interesting if we compare our approach to ShapeConv (Cao et al., 2021). ShapeConv improves the mIoU score by 6% for a cost of 1M additional parameters compared to their already strong 2D baseline (DeepLabv3+). In our case, although we do not reach such high scores, a 1M parameter increase in the number of parameters yields a +12% on the mIoU scores, and the total weight of the network is less than half the weight of ShapeConv.

From these observations, we can conclude that our approach offers competitive performances compared to RGBD approaches (Deeplabv3+, Resnet101 on RGBD (HHA)) with half the number of parameters. However, with new heavier architectures it is possible to obtain better results. Still, our approach outperforms CMX results on the ScanNet validation dataset.

Several reasons explain the relative under-performance of our method on the 2D-3D-S dataset, where heavier architectures are more powerful. For this dataset, we down-sampled the cloud to keep 60% of the points. The feature map is sparser than the depth image used in Cao et al. (2021) or Liu et al. (2022). It is also sparser than the feature maps obtained in the ScanNet dataset. On average, 15% of the pixels have a corresponding point on the ScanNet (10% for the 2D-3D-S).

Table 4. Comparison of the 2D-3D-S dataset. The first line of each block corresponds to the 2D backbone for the methods of the block (except for CMX, which does not provide results on their 2D backbone).

| Methods | InputType | NbParam | 2D baseline | mIoU |
|-----------------------------------|--------------|---------|--------------|-------------|
| U-Net | RGB | 25M | Resnet34 | 41.2 |
| 3D-to-2D distil Liu et al. (2021) | RGB + points | 66M | Resnet34 | 46.42 |
| U-Net + LPointNet (Ours) | RGB + points | 26M | Resnet34 | 53.5 |
| Deeplabv3+ | RGBD (HHA) | 57M | Resnet101 | 54.6 |
| ShapeConv Cao et al. (2021) | RGBD (HHA) | 58M | Resnet101 | 60.6 |
| CMX Liu et al. (2022) | RGBD (HHA) | 140M | SegFormer B4 | 62.1 |

6.3. NYU-V2 dataset

In contrast with the other datasets, NYU-V2 (Nathan Silberman and Fergus, 2012) does not provide a standalone registered point cloud available. But the dataset provides depth images and we can generate a point cloud for each camera using the camera’s intrinsic parameter. We take the raw depth images given by the dataset, as the in-painted version produces a noisy cloud once projected. As a side effect of the per-camera point cloud, the visible points directly correspond to the depth map, and no visibility filter is needed. However, we no longer benefit from 3D information provided by hidden points and we can observe a drop in the quality of the results.

The NYU-V2 dataset provides 795 training images, and 654 validation of indoors scenes annotated with 40 classes. The results are reported in Table 5.

Table 5. 2D mIoU on the validation subset of the NYU-V2 dataset (single scale test).

| Methods | mIoU |
|-----------------------------------|-------------|
| U-Net50 (RGB) | 30.5 |
| LPointNet + U-Net50 (Ours) | 36.5 |
| Segformer-B2 | 46.7 |
| ShapeConv (Cao et al., 2021) | 51.3 |
| CMX(B2) (Liu et al., 2022) | 54.1 |

Compared to the 2D baseline, adding depth information improves the segmentation result. However, the results are far less interesting than when considering a point cloud, as it allows the network to process more contextual information around the points.

6.4. Ablation study

To validate our architecture choices, we perform an ablation study using the validation set of the ScanNet dataset (Dai et al., 2017a), by changing the 3D point feature extraction network or the 2D network. We further tested several modification of the PointNet architecture (see also the supplementary). For this ablation, we remove the data augmentation from the training process to quantify the effect of each modification on the result.

Changing the 2D network. Table 6 reports the performances obtained when using different 2D backbones. Our experiments show that 3D feature information improves the performance of

all ResNet-34, ResNet-50 and DeeplabV3 networks. The performance improvement is particularly significant for ResNet-34. For DeeplabV3 it is less obvious because the network is efficient on images with a better resolution: the images used are 320x240 pixels, while DeeplabV3 preferentially uses 513x513 images during training, to alleviate the effect of image padding on dilated convolution.

Table 6. 2D mIoU on the validation subset of the ScanNet dataset, for our method using Resnet-34, Resnet-50 encoder for U-Net, and DeepLab architecture, using KP-Conv or LPointNet. All results are without data augmentation.

| Methods | mIoU | mIoU gain |
|---------------------------------|-------------|-------------|
| U-Net34 | 55.5 | |
| LPointNet + U-Net-34 | 65.4 | +9.9 |
| KPConv + U-Net-34 | 63.8 | +8.3 |
| U-Net50 | 58.2 | |
| LPointNet + U-Net50 | 65.3 | +7.1 |
| KPConv + U-Net50 | 63.2 | +5. |
| DeepLabV3 ResNet-50 | 60.1 | |
| LPointNet + DeepLabV3 ResNet-50 | 64.5 | +4.4 |

Changing the 3D network. Our approach preferentially relies on PointNet, but it can straightforwardly be adapted with a different 3D neural network. For example one can use KPConv-CNN (Thomas et al., 2019) which uses a ball centered at a query point, a constant sample distribution in this ball and a special convolution on these samples. Since KPConv is memory intensive, we were only able to use a downsampled version of the ScanNet point cloud using Poisson sampling (Cook, 1986) with a query ball of 3cm. On the validation dataset, we obtained a mIoU of 63.8 (see Table. 6). We followed the architecture and data preprocessing given by the KPConv authors without fine tuning it for our case. We set the starting learning rate at 0.001 and add dropout before using the KPConv operation in each encoder layers.

Despite the need of a 3D undersampling, we observe that KPConv improves the performance of a 2D segmentation network. However compared to the LPointNet variation, the number of parameters taken by this approach almost double (27M against 47M). The heavy memory consumption of KPConv goes against our search for a lightweight architecture and this is why we defaulted to LPointNet in all other tests.

Table 7. Effect of using or removing spatial transformers (t-net) on the validation set of the ScanNet Dataset (* denote the addition of data augmentation).

| Methods | mIoU |
|--|-------------|
| PointNet + U-Net | 62.8 |
| PointNet (w/o spatial's t-net) + U-Net | 62.9 |
| PointNet (w/o feature's t-net) + U-Net | 62.6 |
| LPointNet + U-Net (Ours) | 65.4 |
| LPointNet + U-Net34 (Ours)* | 66.1 |

PointNet Architecture choices. In our approach, we chose to remove the spatial transformers from the original PointNet architecture as we observe the cloud from the camera point of view. This 3D orientation is relevant in the scene analysis case, since a floor is likely to be lower than a ceiling, and cannot be vertical. Moreover, it also reduces the weight of the PointNet structure. To validate this experimentally, we compared the performances with and without these spatial transformers, the network being retrained in each case. Table 7 shows that using the spatial transformers degrades the mIoU scores.

Pretraining LPointNet. We test whether pretraining LPointNet can improve the segmentation performance, using a network trained on point sets of 2D-3D-S for 3D semantic segmentation. Table 8 shows that this does not improve the performance. It tends to suggest that the features needed for 3D segmentation might be slightly different than the ones used for helping a 2D segmentation. In the same way, we test the effect of pretraining the 2D encoder on the ImageNet Dataset (Russakovsky et al., 2015). We observe that using a pretrained 2D segmentation network provides a better starting point for the network, allowing it to extract more relevant features on combined feature maps.

Table 8. Effect of using pretrained networks on the validation set of the ScanNet Dataset (* denote the addition of data augmentation).

| Methods | mIoU |
|--|-------------|
| LPointNet + U-Net | 62.5 |
| LPointNet + U-Net (pretrained) (Ours) | 65.4 |
| LPointNet + U-Net (pretrained) (Ours) * | 66.1 |
| LPointNet (pretrained) + U-Net (pretrained) | 64.7 |

6.5. LPointNet feature maps

To illustrate the 3D features extracted by our 2D segmentation driven LPointNet, we show some channels of the features projected on the image plane (Figure 4). Some channels highlight the background (a), other channels highlight flat nearby object surfaces (b) or the floor (c), which hints at the fact that they provide important information for object segmentation.

For more details on the experiments see the supplementary materials.

7. Discussion

While our framework consistently improves 2D segmentation network performances without requiring additional

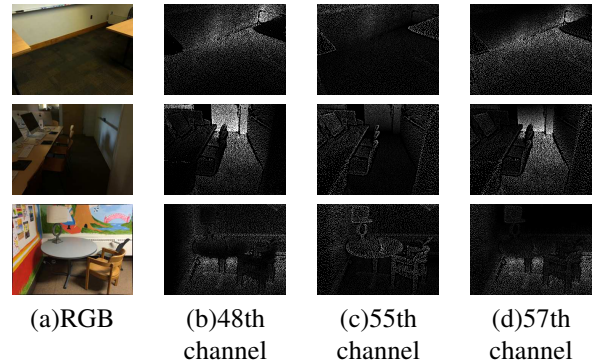


Fig. 4. LPointNet Feature Maps. The different channels of the feature maps highlight various object properties, which explain why they can help the 2D semantic segmentation.

groundtruth labels, some much heavier methods (VirtualMV-Fusion (Kundu et al., 2020), (Liu et al., 2022)) yield better mIoU performances, at the cost of requiring either 3D labels, multi-view images, synthetic data augmentation or a heavier network. Overall, our network exhibits good quantitative performances measured by the mIoU metric (mean Intersection over Union) which is the standard quality measure for segmentation tasks. However, Figure 7 illustrates that this ground truth segmentation is sometimes wrong. For example, some parts have no labels while they should. Our method, aided by 3D geometric features, can better recover the labels in these missing areas, which is good in terms of real performance but is not always reflected in the measured mIoU.

8. Conclusion

In this paper we introduced a 2D segmentation method taking advantage of 3D geometric data without needing explicit 3D network supervision. Our method yields competitive segmentation results, outperforming many other segmentation methods. While we have used our approach for the segmentation of individual images, it is clear that the performances would be further improved by using multiple images, as cross-image label consistency could provide a way to discard wrong labels, a direction we will explore in a future work.

References

- Armeni, I., Sax, A., Zamir, A.R., Savarese, S., 2017. Joint 2D-3D-Semantic Data for Indoor Scene Understanding. ArXiv e-prints arXiv:1702.01105.
- Boulch, A., Guerry, J., Le Saux, B., Audebert, N., 2017. SnapNet: 3D point cloud semantic labeling with 2D deep segmentation networks. Computers and Graphics 71, 189–198. URL: <https://hal.archives-ouvertes.fr/hal-02467932>, doi:10.1016/j.cag.2017.11.010.
- Cao, J., Leng, H., Lischinski, D., Cohen-Or, D., Tu, C., Li, Y., 2021. Shapeconv: Shape-aware convolutional layer for indoor rgb-d semantic segmentation. URL: <https://arxiv.org/abs/2108.10528>, doi:10.48550/ARXIV.2108.10528.
- Chen, L., Papandreou, G., Schroff, F., Adam, H., 2017. Rethinking atrous convolution for semantic image segmentation. CoRR abs/1706.05587. URL: <http://arxiv.org/abs/1706.05587>, arXiv:1706.05587.
- Choy, C., Gwak, J., Savarese, S., 2019. 4d spatio-temporal convnets: Minkowski convolutional neural networks. arXiv:1904.08755.

- Cook, R.L., 1986. Stochastic sampling in computer graphics. *ACM Trans. Graph.* URL: <https://doi.org/10.1145/7529.8927>.
- Dai, A., Chang, A.X., Savva, M., Halber, M., Funkhouser, T., Nießner, M., 2017a. Scannet: Richly-annotated 3d reconstructions of indoor scenes. URL: <https://arxiv.org/abs/1702.04405>, doi:10.48550/ARXIV.1702.04405.
- Dai, A., Nießner, M., 2018. 3dmv: Joint 3d-multi-view prediction for 3d semantic scene segmentation. *arXiv:1803.10409*.
- Dai, J., Qi, H., Xiong, Y., Li, Y., Zhang, G., Hu, H., Wei, Y., 2017b. Deformable convolutional networks. URL: <https://arxiv.org/abs/1703.06211>, doi:10.48550/ARXIV.1703.06211.
- Deng, L., Yang, M., Li, T., He, Y., Wang, C., 2019. Rfbnet: Deep multimodal networks with residual fusion blocks for rgb-d semantic segmentation. URL: <https://arxiv.org/abs/1907.00135>, doi:10.48550/ARXIV.1907.00135.
- Gupta, S., Girshick, R., Arbeláez, P., Malik, J., 2014. Learning rich features from rgb-d images for object detection and segmentation. *arXiv:1407.5736*.
- He, K., Zhang, X., Ren, S., Sun, J., 2015. Deep residual learning for image recognition. URL: <https://arxiv.org/abs/1512.03385>, doi:10.48550/ARXIV.1512.03385.
- Hu, W., Zhao, H., Jiang, L., Jia, J., Wong, T.T., 2021. Bidirectional projection network for cross dimension scene understanding. *arXiv:2103.14326*.
- Hua, B.S., Tran, M.K., Yeung, S.K., 2017. Pointwise convolutional neural networks. URL: <https://arxiv.org/abs/1712.05245>, doi:10.48550/ARXIV.1712.05245.
- Jaritz, M., Gu, J., Su, H., 2019. Multi-view pointnet for 3d scene understanding. *arXiv:1909.13603*.
- Krizhevsky, A., Sutskever, I., Hinton, G.E., 2012. Imagenet classification with deep convolutional neural networks, in: *Proceedings of the 25th International Conference on Neural Information Processing Systems - Volume 1*, Curran Associates Inc., Red Hook, NY, USA. p. 1097–1105.
- Kundu, A., Yin, X., Fathi, A., Ross, D., Brewington, B., Funkhouser, T., Pantofaru, C., 2020. Virtual multi-view fusion for 3d semantic segmentation. URL: <https://arxiv.org/abs/2007.13138>, doi:10.48550/ARXIV.2007.13138.
- Liao, Y., Xie, J., Geiger, A., 2021. KITTI-360: A novel dataset and benchmarks for urban scene understanding in 2d and 3d. *arXiv preprint arXiv:2109.13410*.
- Liu, H., Zhang, J., Yang, K., Hu, X., Stiefelwagen, R., 2022. Cmx: Cross-modal fusion for rgb-x semantic segmentation with transformers. URL: <https://arxiv.org/abs/2203.04838>, doi:10.48550/ARXIV.2203.04838.
- Liu, Z., Qi, X., Fu, C.W., 2021. 3d-to-2d distillation for indoor scene parsing. URL: <https://arxiv.org/abs/2104.02243>, doi:10.48550/ARXIV.2104.02243.
- Liu, Z., Tang, H., Lin, Y., Han, S., 2019. Point-voxel cnn for efficient 3d deep learning. URL: <https://arxiv.org/abs/1907.03739>, doi:10.48550/ARXIV.1907.03739.
- Long, J., Shelhamer, E., Darrell, T., 2014. Fully convolutional networks for semantic segmentation. URL: <https://arxiv.org/abs/1411.4038>, doi:10.48550/ARXIV.1411.4038.
- Long, J., Shelhamer, E., Darrell, T., 2015. Fully convolutional networks for semantic segmentation, in: *Proceedings of the IEEE Conference on Computer Vision and Pattern Recognition (CVPR)*.
- Nathan Silberman, Derek Hoiem, P.K., Fergus, R., 2012. Indoor segmentation and support inference from rgb-d images, in: *ECCV*.
- Pintus, R., Gobbetti, E., Agus, M., 2011. Real-time Rendering of Massive Unstructured Raw Point Clouds using Screen-space Operators, in: Niccolucci, F., Dellepiane, M., Serna, S.P., Rushmeier, H., Gool, L.V. (Eds.), *VAST: International Symposium on Virtual Reality, Archaeology and Intelligent Cultural Heritage*, The Eurographics Association. doi:10.2312/VAST/VAST11/105-112.
- Qi, C.R., Su, H., Mo, K., Guibas, L.J., 2016. Pointnet: Deep learning on point sets for 3d classification and segmentation. URL: <https://arxiv.org/abs/1612.00593>, doi:10.48550/ARXIV.1612.00593.
- Qi, C.R., Yi, L., Su, H., Guibas, L.J., 2017. Pointnet++: Deep hierarchical feature learning on point sets in a metric space. URL: <https://arxiv.org/abs/1706.02413>, doi:10.48550/ARXIV.1706.02413.
- Ronneberger, O., Fischer, P., Brox, T., 2015. U-Net: Convolutional Networks for Biomedical Image Segmentation, in: Navab, N., Hornegger, J., Wells, William M. and Frangi, A.F. (Eds.), *Medical Image Computing and Computer-Assisted Intervention – MICCAI 2015*, Springer International Publishing, Cham. pp. 234–241.
- Russakovsky, O., Deng, J., Su, H., Krause, J., Satheesh, S., Ma, S., Huang, Z., Karpathy, A., Khosla, A., Bernstein, M., Berg, A.C., Fei-Fei, L., 2015. ImageNet Large Scale Visual Recognition Challenge. *International Journal of Computer Vision (IJCV)* 115, 211–252. doi:10.1007/s11263-015-0816-y.
- Su, H., Jampani, V., Sun, D., Maji, S., Kalogerakis, E., Yang, M.H., Kautz, J., 2018. Splatnet: Sparse lattice networks for point cloud processing. *arXiv:1802.08275*.
- Szegedy, C., Liu, W., Jia, Y., Sermanet, P., Reed, S., Anguelov, D., Erhan, D., Vanhoucke, V., Rabinovich, A., 2014. Going deeper with convolutions. URL: <https://arxiv.org/abs/1409.4842>, doi:10.48550/ARXIV.1409.4842.
- Thomas, H., Qi, C.R., Deschaud, J.E., Marcotegui, B., Goulette, F., Guibas, L.J., 2019. Kpconv: Flexible and deformable convolution for point clouds. *arXiv:1904.08889*.
- Valada, A., Mohan, R., Burgard, W., 2019. Self-supervised model adaptation for multimodal semantic segmentation. *International Journal of Computer Vision* 128, 1239–1285. URL: <https://doi.org/10.1007/s11263-019-01188-y>, doi:10.1007/s11263-019-01188-y.
- Wang, W., Neumann, U., 2018. Depth-aware cnn for rgb-d segmentation. *arXiv:1803.06791*.
- Wang, Y., Sun, Y., Liu, Z., Sarma, S.E., Bronstein, M.M., Solomon, J.M., 2018. Dynamic graph cnn for learning on point clouds. URL: <https://arxiv.org/abs/1801.07829>, doi:10.48550/ARXIV.1801.07829.
- Wu, W., Qi, Z., Fuxin, L., 2018. Pointconv: Deep convolutional networks on 3d point clouds. URL: <https://arxiv.org/abs/1811.07246>, doi:10.48550/ARXIV.1811.07246.
- Xie, E., Wang, W., Yu, Z., Anandkumar, A., Alvarez, J.M., Luo, P., 2021. Segformer: Simple and efficient design for semantic segmentation with transformers, in: Ranzato, M., Beygelzimer, A., Dauphin, Y., Liang, P., Vaughan, J.W. (Eds.), *Advances in Neural Information Processing Systems*, Curran Associates, Inc. pp. 12077–12090. URL: <https://proceedings.neurips.cc/paper/2021/file/64f1f27bf1b4ec2292>
- Yu, F., Koltun, V., 2015. Multi-scale context aggregation by dilated convolutions. URL: <https://arxiv.org/abs/1511.07122>, doi:10.48550/ARXIV.1511.07122.
- Zhao, H., Shi, J., Qi, X., Wang, X., Jia, J., 2017. Pyramid scene parsing network, in: *Proceedings of the IEEE Conference on Computer Vision and Pattern Recognition (CVPR)*.

Lightweight integration of 3D features to improve 2D image segmentation *Supplementary material for*

Lightweight integration of 3D features to improve 2D image segmentation

Olivier **PRADELLE**^{c,**}, Raphaëlle **CHAINED**^c, David **WENDLAND**^d, Julie **DIGNE**^c

^cLIRIS, CNRS, Université Lyon 1

^dTechmodigit, 14 Porte du Grand Lyon, Neyron 01700, France

ABSTRACT

This supplementary document gives more details on several aspects of our method. First we detail the data preprocessing step, including an analysis of the visibility filter, and the dependency on the chosen point coordinate system. Then provide a supplementary ablation by moving the merging at different depth and positions in the network. Finally we provide additional segmentation results.

Our code is available at: <https://github.com/OPradelle/2DGuidedLight3D>

1. Data preparation

Our method takes as input a pointset and a picture with known camera pose. We use the camera local frame for the point set coordinates, and to select the points that falls within the camera viewing cone. In this viewing cone, some points might be occluded when observed from the camera viewpoint, and we also compute a visibility filter to select visible points. In this section we detail these data preparation steps.

The ScanNet dataset Dai et al. (2017a) provides images of various scenes, acquired by a RGBD capture system, together with camera poses and the scene’s point cloud. In our case, we use only the RGB frames and the point cloud consolidated from the depth images.

The color images are shot as a video, and are therefore redundant. The amount of images is also expensive in memory which has a strong impact on the training time. To alleviate this issue, we take only an image every 20 frames, resulting in a 95k images subset for the training set.

In addition, some camera poses given in the dataset are corrupted, with invalid values of camera’s parameters, we removed the corresponding frames because our network relies on the correct setting of the camera’s field of view to merge pixels and points features. The ScanNet dataset provides two pointclouds, one dense and one sparse. In order to reduce the training time and memory consumption, we trained the network using the sparse version of the point cloud.

As a preprocessing, we select the points of the scene that fall within the field of view of the camera for each image. Then we use a distance sorting criterion combined with a visibility filter

Pintus et al. (2011) to obtain the subset of points visible in each image. Starting from the projected points on the image plane, following (Pintus et al., 2011), we compute for each projected point the maximum visibility solid angle. If this angle is below a threshold, it means that there is a point that can mask the current point from the camera point of view (see Section 2 for a parameter analysis on the threshold chosen). On average, only 15% of image pixels correspond to projected 3D features. Thus, the geometric feature maps are very sparse images. At the end of the preprocessing, we obtain the field of view points and a sparse image of visible points locations giving geometric context to the corresponding pixels. The 3D encoder uses all the points in the viewing cone to compute features for the visible points. Those features are then merged with the RGB images. In contrast to Hu et al. (2021), our 3D encoder does not rely on a voxelization which inherently loses accuracy. The discretization only occurs when the features are projected on the image plane, but the 3D features exploit the full point set resolution.

2. Parameter analysis for the Visibility threshold

We analyze the effect of the visibility angle parameter in the method of (Pintus et al., 2011). All these experiments are run without any data augmentation.

Table 9 shows that using the visibility filter with a reasonable angle value significantly improves the performance. Figure 5 shows the effect of the visibility threshold on the projected image.

3. 3D coordinate system

(Qi et al., 2016) use spatial transformers to set the points in a canonical position, these spatial transformers being themselves

**Corresponding author:

e-mail: olivier.pradelle@liris.cnrs.fr (Olivier PRADELLE)

Table 9. Visibility angle comparison. A lower angle value mean that more point will be kept by the filter. An angle with a 0 value mean that the nearest point at each pixel will be kept, independently from their 3D position in the scene.

| Visibility angle value | Point-Pixel coverage | mIoU |
|------------------------|----------------------|-------------|
| angle = 0. | 21.5% | 62.3 |
| angle = 2. | 15% | 65.4 |
| angle = 3. | 11.8% | 65.1 |
| angle = 4. | 8.3% | 64.8 |
| angle = 5. | 6.2% | 64.3 |

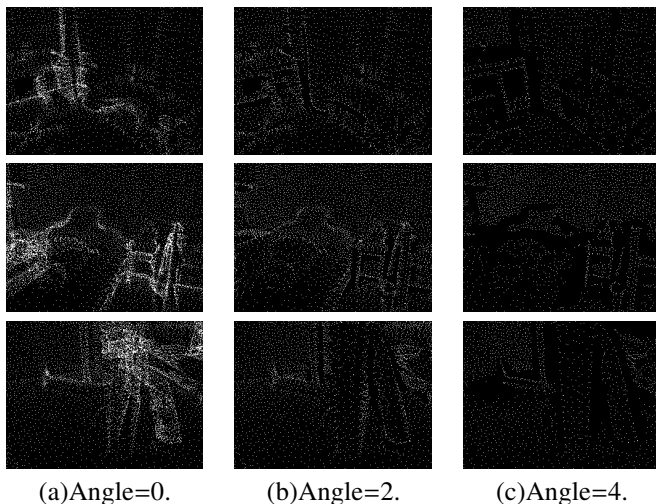


Fig. 5. Effect of the visibility threshold on the projection images.

PointNet instances. In our case, we use the camera’s parameters to set the points in the camera’s coordinate system. Table 10 shows that defining the points coordinates from the camera viewpoint helps the network to extract more relevant features compared to the world coordinate system.

Table 10. Variation on the point’s coordinate system.

| Coordinate system | mIoU |
|--------------------------|-------------|
| World’s system per scene | 63.8 |
| Camera’s system | 65.4 |

4. Merging strategy analysis

We analyse the efficiency of our procedure for merging the 3D features in the 2D image analysis network. We first compare merging such features before the 2D encoder or at the end of the 2D decoder. As illustrated in Table 11, we found that merging the 3D features at an early stage allows the 2D network to better integrate 3D features. Since our 3D network’s weights update comes from the 2D groundtruth, the early merge also helps the 3D network to produce more relevant features for the 2D segmentation task.

To merge the RGB images and the point features images we use two different convolutional layers depending on the availability of a projected 3D information on the pixel. If no point

projects on the pixel, we use a 1x1 convolution to transform it from 3 channels to 64 channels. Otherwise, we concatenate the 61-channel geometric feature with the 3-channel RGB feature and then use a 1x1 convolution to recombine the 64 channels in an optimal way. Another option is to use a single 1x1 convolution operator, independently of the availability of a projected 3D point. In that case we use 0-padding for building a 64 channel descriptor of the projection-less pixels. We call this second option ”Merge with padding”. Table 11 shows that this second option is slightly less efficient.

Table 11. Merging 3D to 2D features using our PointNet variation and a 2D ResNet-34 U-Net network.

| Methods | mIoU |
|---|-------------|
| Late merge (after 2D decoder) | 58.1 |
| Early merge (before 2D encoder) (Ours) | 65.4 |
| Merge with padding | 65.2 |
| Local merge (Ours) | 65.4 |

5. Point cloud visibility

To test the importance of taking into account the visibility, we trained and tested our network on the visible point cloud, containing only the points visible from the camera (removing occluded points), and then the field of view point cloud, containing all points in the camera’s field of view. Importantly enough, even if LPointNet takes as input the field of view points, when projecting the features onto an image at the end of the LPointNet feature extraction, we only retain the features of the visible points, to create the features map.

Table 12 shows that using the field of view points instead of the visible points allows to improve the performance of the network. A reason for this increased performance is that using the field of view point cloud gives stronger characteristics since the points represent the more global context of the images in the 3D scene, rather than just the visible part.

Table 12. Visibility comparison. Using the field of view (FoV) point cloud clearly improves the performances compared to restricting to the visible point cloud. The mIoUs are given for the validation set.

| 3D input | mIoU |
|-------------------------------|-------------|
| Visible point cloud | 62.3 |
| FoV point cloud (Ours) | 65.4 |

6. Point’s features map.

To improve the feature map visualization, we use a PCA on the 61 channel feature maps to extract the 3 most significant channels. Figure 6 shows the RGB, depth images and corresponding PCA feature maps. In the images obtained, we can see that the pixel colors highlight interesting cues such as the distance to the camera and the relative position of the object in the scene. It also shows interesting segmentation cues, giving a same color to an object.

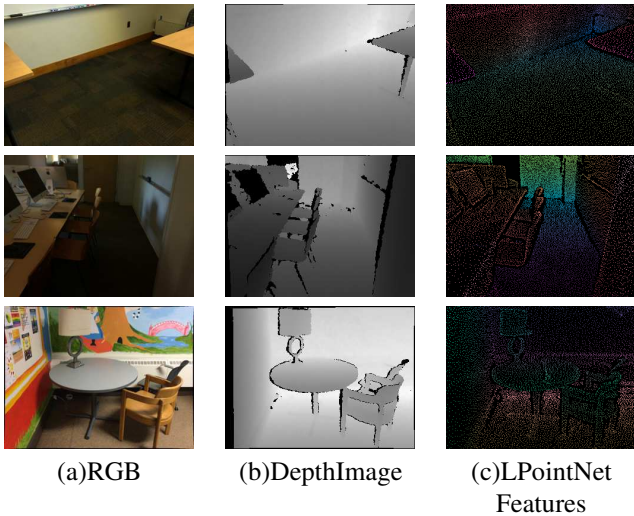


Fig. 6. LPointNet Feature Maps with PCA reduction.

7. Kitti-360

We test our approach on an outdoor dataset, which poses different challenges than indoor scenes, since the field of view can be much larger (possibly infinite). We used the Kitti-360 dataset (Liao et al., 2021). This dataset presents outdoors data captured using fisheye cameras alongside a laser scanning device mounted on a car. The dataset covers a driving distance of 73km with manually annotated images (19 classes). The fisheye images are then rectified yielding a set of registered perspective images. We train and evaluate our approach using the set of perspective images and the point cloud captured at the same time. The dataset is split into a training set of 49k images and a validation set of 12k images. The training and validation set cover different areas of the town.

As the field of view is much larger, capturing a far larger amount of points, we adapt our projection strategy. We first compute the visible points using the camera parameters and the visibility filter similarly to the data preparation procedure of Section 1. We then use a K-NN radius search to gather contextual points around the visible ones. In practice, we first down-sample the point cloud using Poisson sampling (Cook, 1986) with a ball query of 20cm. The K-NN radius search takes points at 1 meter around the visible points.

Table 13 presents the results of our approach compared to our 2D baseline.

Table 13. 2D mIoU on the KITTI-360 validation set. Following the recommended procedure we removed two classes for the evaluation.

| Methods | mIoU |
|-----------------------------------|-------------|
| U-Net | 53.4 |
| LPointNet + U-Net34 (Ours) | 57.5 |

Compared to the indoor datasets, the mIoU is still clearly improved but the gain is smaller. Indeed, the large field of view combined with visibility and neighborhood selection yield a point set which is much more disconnected than the ones for the indoor scenes. More precisely, it gives a set of clusters of

points distant from each other. This difference in point distribution might require some network adaptation, but this deserves further investigations.

The Kitti360 is a relatively new dataset, the associated benchmark shows two 2D-only methods giving good performances, including a VGG16-FCN (Long et al., 2015) with a mIoU score of 54%, the other network is attention-based (Zhao et al., 2017) and reaches 64% as mIoU. These scores are only given as a guide since they are provided on the test set, while we performed our experiments on the validation set (access to the test set requiring a heavy procedure). VGG16-FCN seems to yield a comparable (or a little smaller) score to our method, but it is much heavier (134M vs 26M parameters in our case).

The attention-based network clearly outperforms our method, but this result was expected. Networks using attention mechanisms give better results on outdoor datasets due to the object scales. A same object can indeed appear at very different scales in outdoor datasets as a consequence of the large depth field captured by the RGB images, a scale discrepancy that is very well handled by attention mechanisms.

8. More segmentation result

We provide more segmentation result on the ScanNet (Dai et al., 2017a) dataset in Figure 7.

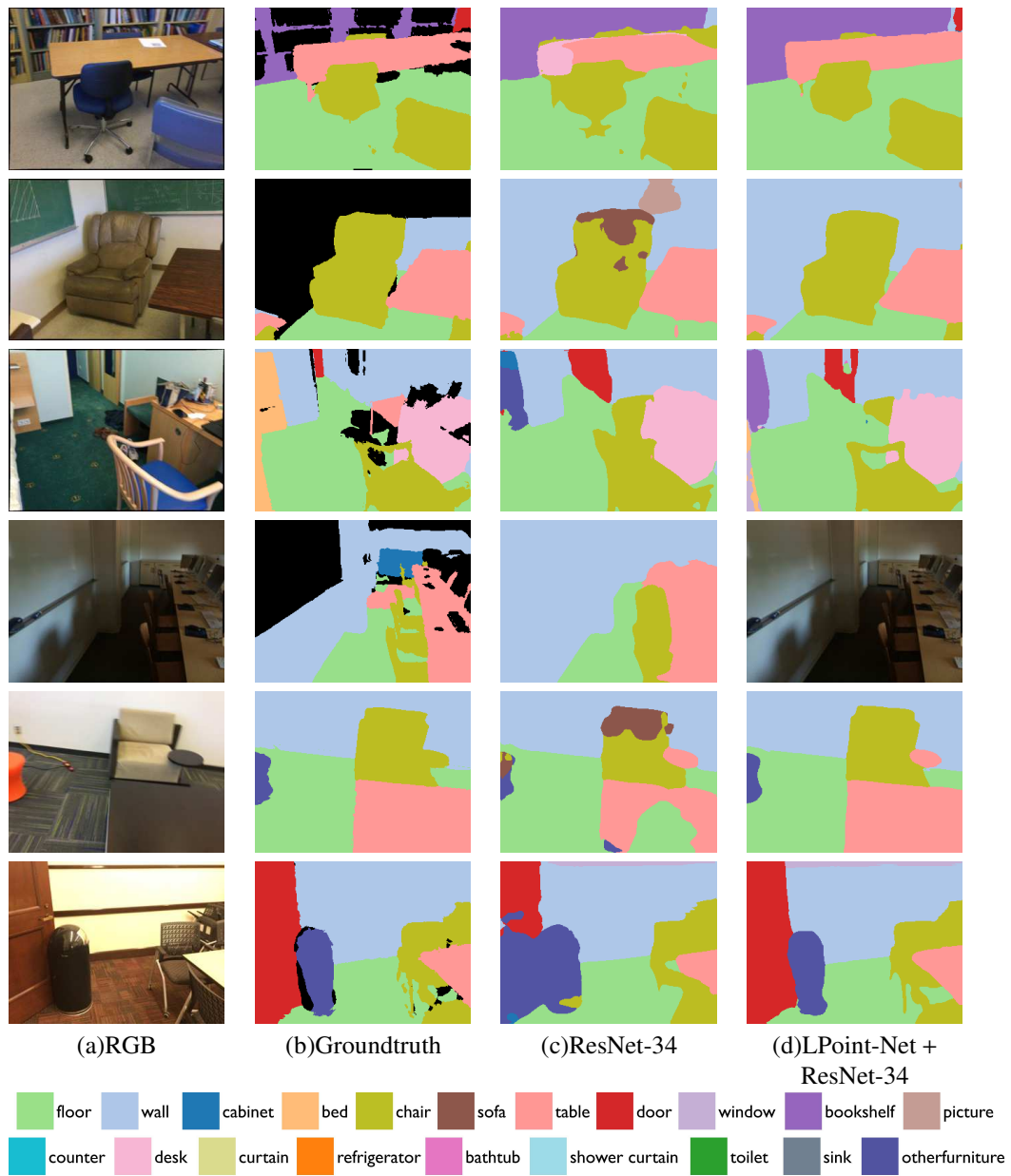


Fig. 7. Segmentation result on the ScanNet validation dataset.